Virology 517 (2018) 98–107

Contents lists available at ScienceDirect

Virology

journal homepage: www.elsevier.com/locate/virology

# Adaptive evolution influences the infectious dose of MERS-CoV necessary to achieve severe respiratory disease

Madeline G. Douglas[a], Jacob F. Kocher[a], Trevor Scobey[a], Ralph S. Baric[a,b,1], Adam S. Cockrell[a,*,1]

[a] Department of Epidemiology, University of North Carolina-Chapel Hill, Chapel Hill, NC 27599, USA
[b] Department of Microbiology and Immunology, University of North Carolina-Chapel Hill, Chapel Hill, NC 27599, USA

## ARTICLE INFO

*Keywords:*
Coronavirus
MERS-CoV
Middle East respiratory syndrome
Respiratory disease
Acute respiratory distress syndrome
Spike protein

## ABSTRACT

We recently established a mouse model (288–330$^{+/+}$) that developed acute respiratory disease resembling human pathology following infection with a high dose ($5 \times 10^6$ PFU) of mouse-adapted MERS-CoV (icMERSma1). Although this high dose conferred fatal respiratory disease in mice, achieving similar pathology at lower viral doses may more closely reflect naturally acquired infections. Through continued adaptive evolution of icMERSma1 we generated a novel mouse-adapted MERS-CoV (maM35c4) capable of achieving severe respiratory disease at doses between $10^3$ and $10^5$ PFU. Novel mutations were identified in the maM35c4 genome that may be responsible for eliciting etiologies of acute respiratory distress syndrome at 10–1000 fold lower viral doses. Importantly, comparative genetics of the two mouse-adapted MERS strains allowed us to identify specific mutations that remained fixed through an additional 20 cycles of adaptive evolution. Our data indicate that the extent of MERS-CoV adaptation determines the minimal infectious dose required to achieve severe respiratory disease.

## 1. Introduction

Middle East respiratory syndrome is an emerging viral respiratory infection caused by Middle East respiratory syndrome coronavirus (MERS-CoV), first identified in Saudi Arabia in 2012. This novel coronavirus is associated with severe pneumonia and acute respiratory distress syndrome (ARDS) that often results in mortality (~ 35%) (Alsaad et al., 2017; Arabi et al., 2017; Ng et al., 2016). Over 2100 cases and 733 deaths have been reported in twenty-seven countries through December 2017, all geographically linked to the Middle East (WHO, 2017). Though sporadic infections and small nosocomial outbreaks continue to occur across the Arabian Peninsula, the potential for global transmission was demonstrated by an outbreak in South Korea in 2015 (Arabi et al., 2017). Spread from a single infected individual returning from the Arabian Peninsula resulted in 186 confirmed cases with a ~ 20% mortality rate (Lee, 2015). Current treatment for MERS-CoV relies on supportive treatment of symptoms, with potential MERS-CoV therapeutic countermeasures gradually progressing toward clinical trials.

Developing therapeutic strategies has been hindered by a poor understanding of viral pathogenesis in humans, which has created challenges in developing applicable animal models that resemble the human disease outcomes. Only recently have there been two case reports describing the pathological consequences observed in MERS-CoV infected patients (Alsaad et al., 2017; Ng et al., 2016). Non-human primates (NHPs) offer advantages in preclinical therapeutic testing due to their physiological similarities to humans. Two NHP models (rhesus macaques and marmosets) were shown to support MERS-CoV infection; however, there are limitations with regard to the ability to detect replicating MERS-CoV in the lungs and the extent of respiratory disease appears to vary from mild-to-severe in a laboratory dependent manner (Chan et al., 2015; Falzarano et al., 2014; Johnson et al., 2016, 2015; Munster et al., 2013). Importantly, this may be a consequence of difficulty in establishing MERS-CoV infection in the lower respiratory tract, where the dipeptidyl peptidase 4 (DPP4) receptor is predominantly expressed in the human respiratory tract (Meyerholz et al., 2016), or potential species-specific differences in DPP4 signaling mechanisms may impact production of high titer MERS-CoV. Complexities in establishing infection in NHPs suggest that MERS-CoV may not be adapted to elicit the severe respiratory disease often associated with human infections. MERS-CoV adaptation by repeated passage within these NHP species may help to enhance virulence and replicate severe human disease reliably in NHPs.

Species adaptation has shown to be previously successful in establishing MERS-CoV infection that elicited lethal respiratory disease in two humanized mouse models (Cockrell et al., 2016; Li et al., 2017a). Cockrell et al. utilized CRISPR–Cas9 (clustered regularly interspaced

---

[*] Corresponding author.
[1] Co-Senior authors.

https://doi.org/10.1016/j.virol.2017.12.006
Received 30 September 2017; Received in revised form 6 December 2017; Accepted 11 December 2017

short palindromic repeats and CRISPR-associated gene 9) technology to make amino acid substitutions at positions 288 and 330 of mDPP4 to generate a humanized mouse model (288–330 $^{+/+}$) that supported high levels of virus replication. Fifteen serial passages of virus in heterozygous 288–330$^{+/-}$ mice resulted in a mouse-adapted virus (icMERSma1) capable of achieving dramatic weight loss, severe lung pathology, and lethal respiratory disease in 288–330$^{+/+}$ mice. Importantly, minimizing changes to the mDPP4 precluded disruption of its innate role in glucose homeostasis and immune dysregulation (Ohnuma et al., 2008; Rohrborn et al., 2015). By replicating clinical disease, while also preserving host-specific DPP4 expression patterns and immune functionality, this humanized mouse model offers a useful tool to study pathogenesis and therapeutic testing.

A limitation of the icMERSma1 virus was the high dose (5 × $10^6$ PFU) required to produce severe respiratory disease through the intranasal route of infection (Cockrell et al., 2016); whereas, other MERS-CoV mouse models demonstrated that disease could be achieved at lower infectious doses (Coleman et al., 2017; Li et al., 2017a). Evidence in MERS-CoV infected patients indicates that there may be an association between virus dose and the severity of respiratory disease (Oh et al., 2016). Initiating disease through natural acquisition of MERS-CoV may also be dose dependent. Therefore, to achieve a dose that more closely resembles a naturally acquired infection we continued the adaptive evolution of icMERSma1 in 288–330$^{+/-}$ mice. We generated a novel mouse-adapted MERS-CoV clone (maM35c4) that confers pathology indicative of severe respiratory disease at substantially lower doses in 288–330$^{+/+}$ mice. Mouse-adapted M35c4 causes pathology similar to icMERSma1, but exhibited dose-dependent effects at $10^3$–$10^5$ PFU. We identified unique mutations in the maM35c4 clone that may promote severe respiratory disease at 10–1000 fold lower virus doses than previously observed. Most notably, comparative genetics of maM35c4 and icMERSma1 provided us a distinct advantage by allowing us to identify mutations that remained fixed after an additional 20 passages, implicating their importance in conferring virulence in mice.

## 2. Results

### 2.1. Evolving MERS-CoV in mouse lung maintains disease at lower infectious doses

MERS-CoV was mouse-adapted by serial passage through the lungs of the heterozygous, 288–330$^{+/-}$ mice as previously described (Cockrell et al., 2016). Fatal disease was routinely observed at the 5 × $10^6$ PFU dose (Cockrell et al., 2016), a potential limitation that could be overcome through continued passaging through the lungs of 288–330$^{+/-}$ mice (Cockrell et al., 2016). Here, we demonstrate that continued passaging of the icMERSma1 virus through the lungs of 288–330$^{+/-}$ mice yielded mouse-adapted MERS strains that exhibited dramatic weight loss after 25 and 35 passages, respectively referred to as maMERS-25 and maMERS-35. The two heterogeneous mouse-adapted MERS-CoV populations (maMERS-25 and maMERS-35) were expanded in CCL81 Vero cells and tested at 5 × $10^4$ and 5 × $10^5$ PFU doses by intranasal inoculation of the 288–330$^{+/+}$ mice (Fig. 1). Significant weight loss was observed through day 8 post-infection (p.i.) at two different doses. Mouse-adapted maMERS-35 exhibited the most significant weight loss at both 5 × $10^4$ PFU and 5 × $10^5$ PFU with average weight loss of > 20% at both doses (Figs. 1a and 1b). Notably, all mice were euthanized as they approached our 30% weight exclusion limit. We anticipate that these mice would have succumbed to disease at later times post-infection. In contrast, the mice infected with maMERS-25 only reached 16–22% weight loss (Figs. 1a and 1b), indicating that maMERS-25 may be less virulent than maMERS-35. Despite the differences in disease severity, increased passaging resulted in two novel MERS-CoV heterogeneous virus populations that elicit weight loss, which is commonly associated with severe respiratory disease. These data indicate that novel virus genetic mutations were acquired during additional rounds of adaptation in the 288–330$^{+/-}$ mice. To gain insight into these genetic changes plaque purification was used to isolate a novel clone from the more virulent maMERS-35.

### 2.2. A clonal isolate of maMERS-35 induces fatal respiratory disease in 288–330$^{+/+}$ mice

A clonal isolate (maM35c4) was derived from a plaque purified virus of maMERS-35 on CCL81 Vero cells. 288–330$^{+/+}$ mice were intranasally infected with three different doses of maM35c4 (5 × $10^3$, 5 × $10^4$, and 5 × $10^5$ PFU) (Fig. 2). Severe weight loss (> 20%) was associated with 5 × $10^4$ and 5 × $10^5$ PFU by day 7 p.i., with little weight loss at the 5 × $10^3$ PFU dose (Fig. 2a). Significant mortality (50% succumbed to disease during the course of the experiment) was observed at the 5 × $10^5$ PFU dose, whereas all animals survived through day 7 p.i. at the 5 × $10^4$ and 5 × $10^3$ PFU doses (Fig. 2b). Graphing survival at 20% or 30% weight loss demonstrates decreased survival at 5 × $10^3$ and 5 × $10^4$ PFU doses (Supplementary Fig. 1). However, all mice were euthanized as mice receiving 5 × $10^4$ and 5 × $10^5$ PFU doses approached our 30% weight exclusion limit. Based on these results we would suggest an $LD_{50}$ of ~ 1–2 × $10^4$ PFU. Dramatic weight loss and mortality correlated well with severe respiratory disease as quantified by gross investigation of hemorrhaging in the lungs at days 3 and 7 post-infection (Fig. 2c). Lungs were scored for hemorrhaging on a scale of 0 (no hemorrhaging) to 4 (severe hemorrhaging) throughout all lung lobes. Early after infection (day 3 p.i.), hemorrhage scores correlated with the dose of virus administered (Fig. 2c). Compared to minor hemorrhaging at 5 × $10^3$ PFU, both the 5 × $10^4$ and 5 × $10^5$ infectious doses elicited significant hemorrhaging at day 3 p.i. (Fig. 2c). By day 7 p.i. 5 × $10^4$ and 5 × $10^5$ PFU doses invoked dramatic hemorrhaging across all lung lobes (Fig. 2c). Interestingly, although minimal weight loss occurred in mice infected with 5 × $10^3$ PFU dose, substantial lung hemorrhaging was observed by day 7 p.i., indicating that the 5 × $10^3$ dose of maM35c4 causes significant lung disease (Fig. 2c). The viral loads in the lungs are consistent with the disease elicited by the different doses (Fig. 2d). At day 3 p.i. maMERS35c4 replicated to high titers ($10^8$–$10^9$ PFU/ml/gram lung tissue) in the lungs at all doses, with mean lung titers increasing with increased dose (Fig. 2d). Titers at day 7 p.i. exhibited a dose-dependent effect on clearance of maM35c4 from the lungs (Fig. 2d). Mice infected with 5 × $10^3$ PFU dose show little to no detection of virus at day 7 p.i., while higher titers persist in mice infected at both 5 × $10^4$ and 5 × $10^5$ PFU doses (Fig. 2d). Weight loss, mortality, hemorrhaging and viral load in the lungs are consistent with a dose-dependent effect on MERS-CoV-induced disease. Lung disease by gross hemorrhaging was observed at doses as low as 5 × $10^3$ PFU, indicating that infection elicited dramatic pathological changes in the lung architecture.

### 2.3. maM35c4 causes widespread infection of the lungs and pathology characteristic of acute respiratory distress syndrome (ARDS)

MERS-CoV viral loads in the lungs of infected humans exhibit a phased correlation with the development of respiratory disease. Viral loads peak early after infection and as viral loads begin to decrease, symptoms associated with respiratory disease increase (Oh et al., 2016). A similar correlation was observed following infection of 288–330$^{+/+}$ mice with maM35c4. Mouse-adapted M35c4 reached peak viral loads shortly after infection (3 days p.i.), and began to resolve at late times post-infection (7 days p.i.) (Fig. 2d and Fig. 3). MERS-CoV nucleocapsid antigen staining by immunohistochemistry revealed widespread infection of the lungs at day 3 p.i. at all three doses and substantial clearance by day 7.p.i., affecting both the parenchyma and airway epithelium (Fig. 3 and Table 1). This corresponds well with the dose-dependent effect of viral loads in the lungs (Fig. 2d). Consistent with viral replication peaking early by day 3 p.i. the initial signs of lung pathology

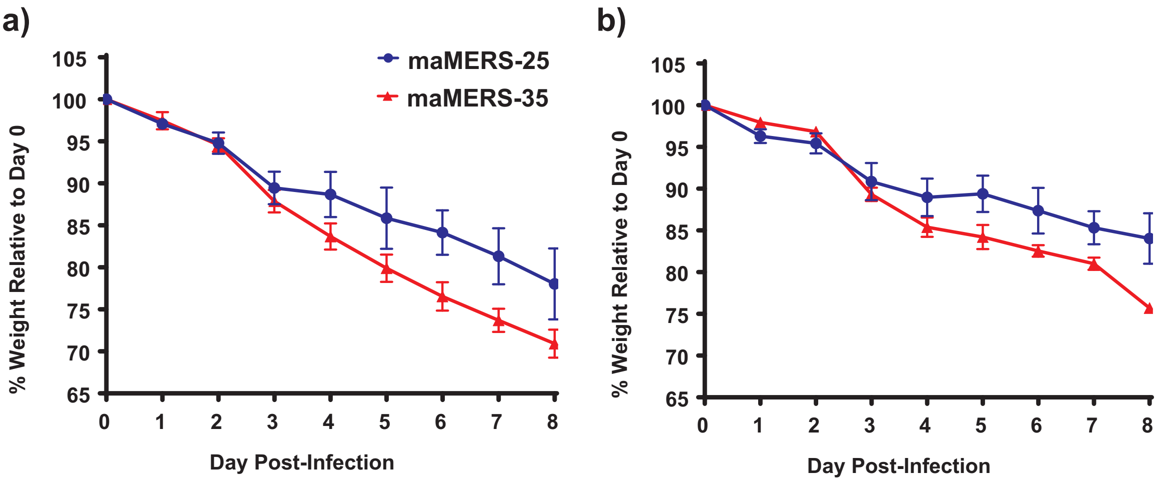

**Fig. 1. MERS-35 elicits enhanced disease at decreased viral doses.** a. Mouse weights were measured daily up to day 8 p.i. for 288–330$^{+/+}$ mice infected intranasally with 5 × $10^5$ PFU MERS-25 ($n$ = 3, blue circles) or MERS-35 ($n$ = 3, red triangles). b. Mouse weights were measured daily up to day 8 p.i. for 288–330$^{+/+}$ mice infected intranasally with 5 × $10^4$ PFU MERS-25 ($n$ = 3) or MERS-35 ($n$ = 3). All data are daily means of the percent weight relative to day 0 ± S.E.M.

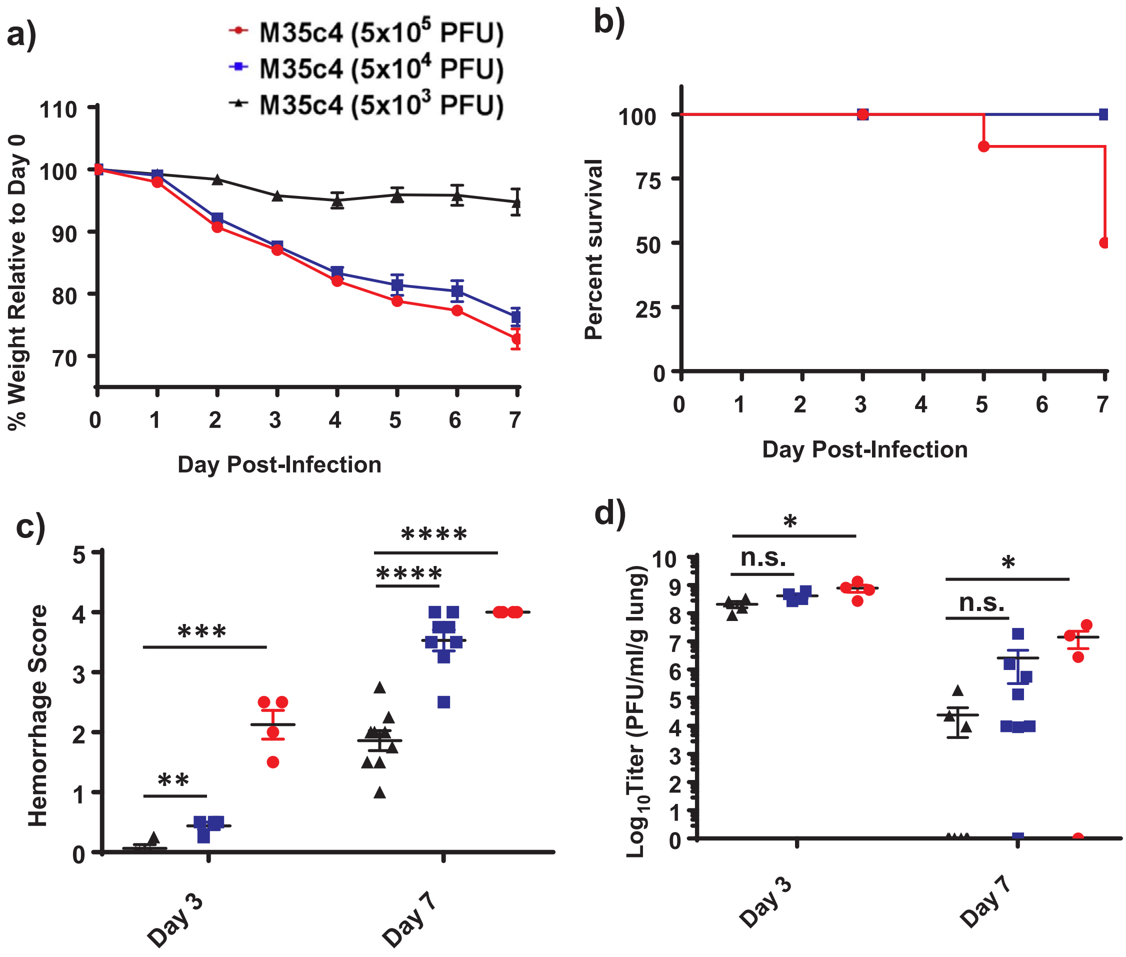

**Fig. 2. Mouse-adapted M35c4 exhibits significant respiratory disease at low infectious doses.** Mice were infected intranasally with 5 × $10^3$ ($n$ = 13, black triangles), 5 × $10^4$ ($n$ = 12, blue squares), or 5 × $10^5$ ($n$ = 12, red circles) PFU of maM35c4. Mice were monitored daily for weight loss (a) and survival (b). The severity of hemorrhage was scored on a scale of 0 (no hemorrhage) to 4 (complete hemorrhage) (c), and lung titers were measured (d), for 288–330$^{+/+}$ mice infected with the 5 × $10^3$ dose at day 3 p.i. ($n$ = 4) and day 7 p.i. ($n$ = 9), 5 × $10^4$ dose at day 3 p.i. ($n$ = 4) and day 7 p.i. ($n$ = 8), and 5 × $10^5$ dose at day 3 p.i. ($n$ = 4) and day 7 p.i. ($n$ = 4). All data are represented as means ± S.E.M. For lung titers below the limit of detection values were set at 1 to depict those mice on the graph.

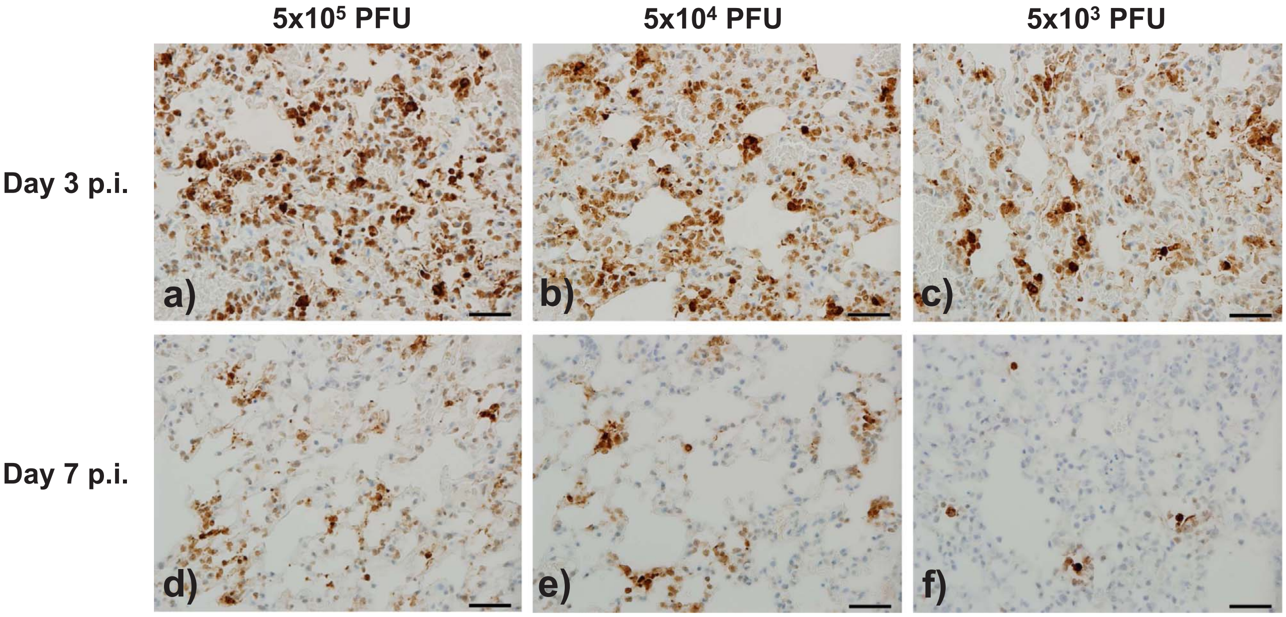

**Fig. 3. Immunohistochemistry reveals high levels of maM35c4 infection in 288–330$^{+/+}$ mouse lungs.** Mouse lung sections were stained for MERS-CoV nucleocapsid antigen to identify lung cells positive for maM35c4 infection. Representative images are shown for lung sections from mice infected with doses of 5 × $10^5$ (a,d), 5 × $10^4$ (b,e), or 5 × $10^3$ (c,f) PFU at 3 days and 7 days p.i. All images were acquired at 40X magnification. Images are representative of at least 3 samples. Scale bars in lower right corners of each panel are 1 mm.

were observed by day 3 p.i. (Table 1), with ARDS-related pathological changes most prevalent at day 7 p.i. (Fig. 4 and Table 1). Changes in lung architecture were most dramatic in mice infected with 5 × $10^5$ PFU (Fig. 4a-d). Quantitative assessment of hyaline membrane formation exhibits a clear dose related phenotype, with most dramatic disease exhibited at the 5 × $10^5$ PFU dose (Table 1). A low magnification image of a large airway showed denuding of the epithelial cell layer when viewed from left-to-right, debris in the airway, severe polynuclear infiltration in the alveoli and alveoli ducts, and hyaline membrane formation, reflecting many of the exhibited pathologies noted in human cases with severe acute respiratory distress syndrome (Fig. 4a-d). Although hyaline membrane formation was less frequent in mice at the 5 × $10^4$ PFU dose, severe inflammation, intra-alveolar edema, denuding of large airways and cellular debris in large airways was readily observed (Fig. 4e-h). Consistent with the dramatic gross hemorrhaging observed at the 5 × $10^4$ PFU and 5 × $10^5$ PFU doses (Fig. 2c), red blood cells were frequently detected in the large airways, and alveolar spaces (Fig. 4c,f,h). Interestingly, despite the mild weight loss observed at the 5 × $10^3$ PFU dose (Fig. 2a), mice exhibited respiratory pathology consistent with respiratory disease including intra-alveolar edema, perivascular cuffing, and severe inflammation (Fig. 4i-k and Table 1), although many areas displayed normal lung morphology (Fig. 4l). Our results indicate that maM35c4 elicited dose-dependent pathological changes, primarily hyaline membrane formation, in the lower respiratory tract that reflect a loss of respiratory function, and are commensurate with weight loss, increased mortality, and increased hemorrhaging in the lungs of infected 288–330$^{+/+}$ mice. Achieving dramatic disease at 5 × $10^5$ and 5 × $10^4$, and to a lesser extent at 5 × $10^3$ PFU, demonstrates that severe respiratory disease was comparable to that seen at 5 × $10^6$ PFU for icMERSma1, and suggests that maM35c4 acquired additional mutations that enhanced virulence.

### 2.4. Identification of MERS-CoV- mutations acquired during adaptation

Sequencing the genome of the plaque purified maM35c4 revealed several unique mutations acquired during serial passaging, including a single nucleotide change in the 5′ UTR and single amino acid changes in nonstructural proteins nsp3, nsp6, nsp8 and nsp14 (Table 2). Novel single amino acid changes were also observed in the spike protein, orf3, orf4a, and membrane proteins (Table 2). Additionally, maM35c4 acquired a large deletion extending from orf4b through the beginning of orf5 (Table 2). Though unique, mutations in 5′ UTR, nsp6, nsp8, spike protein, and Orf4b were also present in the previously adapted icMERSma1 virus (Cockrell et al., 2016). Most notable are the mutations that remained after the additional 20 rounds of adaption to achieve the maM35c4 virus, nsp8 (I108L), spike insertion of RMR, and spike mutation of S885L [Table 2 and (Cockrell et al., 2016)], implicating these mutations as critical for eliciting respiratory disease in our mouse model. Although maM35c4 mutations in the 5′UTR and nsp6 are different from those in the icMERSma1 virus, acquiring novel mutations in the same viral genetic domains implicates the 5′UTR and nsp6 as important regions for MERS-CoV to elicit respiratory disease in our 288–330$^{+/+}$ mouse model. In contrast, mutations acquired in orf3, orf4b, and orf5 indicate that their function is expendable for maM35c4 to elicit respiratory disease. Importantly, the N222Y spike mutation is notably similar to an N222D mutation that was acquired by a mouse-adapted MERS-CoV described in a recent study (Li et al., 2017a). Our sequencing results demonstrate that the spike mutations are all highly conserved mouse-adaptations between strains from our lab (Insertion RMR and S885L), as well as strains between labs [N222Y for maMERS35c4 and N222D from (Li et al., 2017a)]. The conserved nature of these mouse-adapted mutations prompted us to investigate their potential in altering structuring features of the MERS-CoV spike using structural prediction software to place these mutations in the context of the spike trimer.

### 2.5. Structural comparison of maM35c4 spike mutations

Homology based structural modeling was used to understand how the conserved mouse-adapted spike mutations may influence the structure of the MERS-CoV trimers when placed on the prefusion spike trimer determined by Yuan et al. (2017) using cryo-EM . The maM35c4 spike mutations identified in this study and MA2.0 mutations identified by Li et al. (2017a) were compared to the S1 and S2 domains of spike from EMC 2012 (Fig. 5a). Each of the spike mutations indicated in Fig. 5a, and Table 1, was placed onto each monomer of the MERS-CoV spike trimer (Fig. 5b). Using the freely available prediction software (NetNGlyc 1.0 Server) it seemed likely that N222 is a putative

**Table 1**
Lung histopathology from maM35c4-infected 288–330+/+ mice.

| | | IHC Scoring | | Airway Inflammation | | | Vasculature | | Parenchyma (Alveoli) | | Diffuse Alveolar Damage | | Eosinophils |
|---|---|---|---|---|---|---|---|---|---|---|---|---|---|
| Viral Dose | Day Post Infection | Airway | Parenchyma | Denudation | Debris | Inflammation | Perivascular Cuffing | Edema | Interstitial Septum | Airspace Inflammation | Hyaline Membrane | Exudates | |
| $5 \times 10^5$ PFU | Day 3 ($n = 4$) | 0.75 ± 0 | 2.69 ± 0.47 | 0.25 ± 0 | 0.69 ± 0.13 | 0.69 ± 0.13 | 0.94 ± 0.13 | 0.38 ± 0.14 | 0.81 ± 0.38 | 1.19 ± 0.24 | 0.00 ± 0 | 0.94 ± 0.52 | 0.31 ± 0.13 |
| | Day 7 ($n = 4$) | 0.34 ± 0.19 | 0.84 ± 0.49 | 0.38 ± 0.14 | 0.69 ± 0.24 | 0.75 ± 0.35 | 1.31 ± 0.13 | 0.69 ± 0.24 | 0.75 ± 0.20 | 1.13 ± 0.48 | 1.56 ± 1.05 | 0.25 ± 0 | 0.50 ± 0 |
| $5 \times 10^4$ PFU | Day 3 ($n = 4$) | 0.50 ± 0 | 1.75 ± 0.54 | 0.31 ± 0.13 | 0.69 ± 0.59 | 0.50 ± 0.29 | 1.00 ± 0.35 | 0.31 ± 0.24 | 0.81 ± 0.38 | 0.75 ± 0.41 | 0.06 ± 0.13 | 0.75 ± 0.35 | 0.31 ± 0.13 |
| | Day 7 ($n = 8$) | 0.11 ± 0.12 | 0.45 ± 0.44 | 0.25 ± 0 | 0.69 ± 0.26 | 0.88 ± 0.19 | 1.41 ± 0.40 | 0.53 ± 0.16 | 0.94 ± 0.18 | 1.50 ± 0.50 | 0.31 ± 0.51 | 0.41 ± 0.30 | 0.78 ± 0.28 |
| $5 \times 10^3$ PFU | Day 3 ($n = 4$) | 0.50 ± 0 | 1.75 ± 0.20 | 0.25 ± 0.20 | 0.56 ± 0.38 | 0.44 ± 0.24 | 0.69 ± 0.13 | 0.19 ± 0.24 | 0.63 ± 0.14 | 0.50 ± 0.29 | 0.00 ± 0 | 0.13 ± 0.14 | 0.44 ± 0.24 |
| | Day 7 ($n = 9$) | 0.01 ± 0.04 | 0.13 ± 0.15 | 0.33 ± 0.18 | 0.69 ± 0.53 | 0.81 ± 0.27 | 1.44 ± 0.37 | 0.72 ± 0.23 | 1.33 ± 0.43 | 1.69 ± 0.41 | 0.00 ± 0 | 1.44 ± 0.72 | 0.50 ± 0 |
| [a]Mock | Day 7 ($n = 3$) | 0.04 ± 0.07 | 0.08 ± 0.07 | 0.00 ± 0 | 0.00 ± 0 | 0.08 ± 0.14 | 0.21 ± 0.26 | 0.00 ± 0 | 0.25 ± 0.25 | 0.00 ± 0 | 0.00 ± 0 | 0.00 ± 0 | 0.00 ± 0 |

Disease scoring is based on a scale of 0–3 (0 = none and 3 = severe). Each value represents the mean ± standard deviation.

[a] Mock mouse lungs were independently processed for purposes of histological comparison.

glycosylation site. Though the N222Y mutation occurred at the same position as the N222D mutation in the N-terminal domain, replacing the polar amino acid N with a nonpolar, uncharged Y residue appears to result in a slight structural modification; whereas, the N222 structural feature appears to be maintained in the context of the negatively charged D residue (Fig. 5b,d). Also highlighted on the trimer spike structures are the RMR insertion and the S885L spike mutations in the S2 domain (Fig. 5b), which were conserved across the maM35c4 and icMERSma1 strains. Interestingly, the maM35c4 RMRL mutations (red) directly overlap with part of the S2′ fusion domain (yellow), and apparently alters the S2′ furin cleavage site (Millet and Whittaker, 2014) (Fig. 5c, green). Using freely available furin cleavage site prediction software (ProP 1.0 Server) we determined that insertion of RMR most likely generated a novel furin cleavage site. The mouse-adapted mutations in spike may have important implications regarding enhancing viral replication and determining tropism, but ARDS-like respiratory disease is most likely dependent on the combination of spike mutations and conserved mutations that we have identified at other MERS-CoV genetic loci.

## 3. Discussion

### 3.1. Adaptive evolution influences MERS-CoV virulence

This study found that extending the passage of MERS-CoV through $288–330^{+/-}$ mice enhanced virulence, achieving severe respiratory disease at 10–1000 fold lower doses than those seen with earlier passage 15 viruses (Cockrell et al., 2016). Continued adaptive evolution for an additional 20 rounds generated maM35c4, which is capable of eliciting comparable levels of disease at significantly lower doses ($10^3$ – $10^5$ PFU). The ability to use lower challenge doses more likely reflects MERS-CoV infection in humans. Nosocomial transmissions have been the primary source of outbreaks [reviewed in (Arabi et al., 2017)]. Importantly, individuals that are older (> 50), and/or those that have co-morbidities (*e.g.* diabetes, hypertension, *etc.)* are at higher risk of severe disease. Therefore, individuals presenting with pre-existing conditions may be more susceptible to disease at lower viral doses. A recent study demonstrated that the patient room environment (*e.g.* bed sheets, bed rails, IV fluid hangers, radiography cassettes and anteroom tables) in the healthcare setting was readily contaminated with replication competent MERS-CoV (Bin et al., 2016). MERS-CoV was detected on numerous additional surfaces by RT-PCR, indicating contamination throughout patient rooms (Bin et al., 2016). Although it is not clear what dose of virus is necessary to establish infection and disease in humans, it is not unlikely that low dose contaminated environmental sources contributes to hospital transmission. Thus, evaluating a broad range of dosing options ($10^3$–$10^7$) in our mouse model affords us the unique ability to investigate at least three independent lines of research: i) how varying infectious dose influences MERS-CoV pathogenesis; ii) therapeutic efficacy at different infectious doses; and iii) comparative genetics of different mouse-adapted strains to investigate MERS-CoV genetic correlates of respiratory disease.

Comparative genetics of the mouse-adapted icMERSma1 virus (15 passages) with maM35c4 (35 passages) provides insight into how adaptive evolution augments virulence of MERS-CoV in a mouse model. In addition to a number of novel mutations we identified specific mutations in the maM35c4 virus that remain conserved through an additional 20 passage, and may be instrumental for conferring severe respiratory disease in mice. Furthermore, we identified a missense mutation site in the spike protein that was independently identified in a different model of adaptive evolution (Li et al., 2017a), implicating this site as central to enhanced MERS-CoV pathogenesis in the mouse. We also observed mutations in multiple nonstructural proteins, structural proteins, and several orf's that may influence MERS-CoV pathogenesis through enhanced viral fidelity and/or evasion of host immune responses.

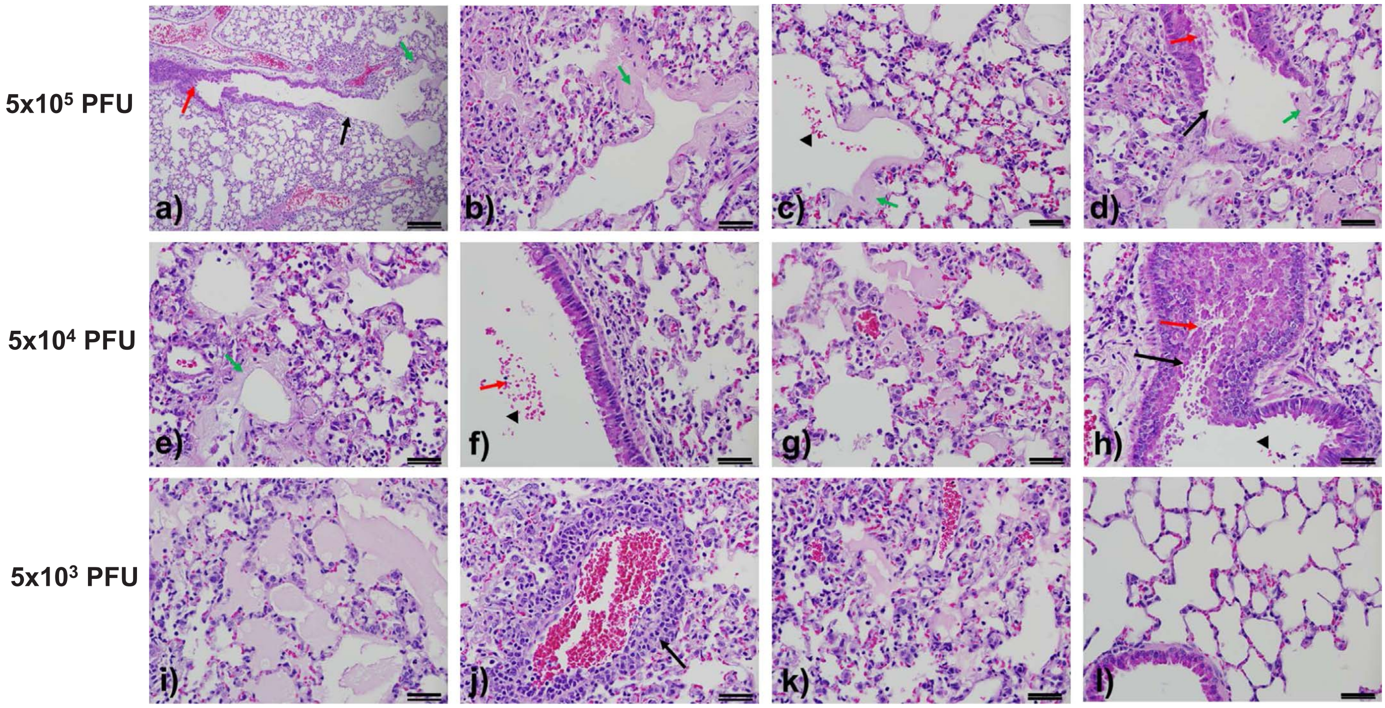

**Fig. 4. Mouse-adapted M35c4 elicits pathology associated with ARDS.** Representative images were acquired from mouse lungs infected with maM35c4 at doses of $5 \times 10^5$ (a-d), $5 \times 10^4$ (e-h), or $5 \times 10^3$ (i-l) PFU at day 7 p.i. Images reflect the severity of disease observed at the different doses including denuding of large airways (a, d, h), debris in the airways (a, d, f, h), hyaline membranes (a-e), red blood cells in the large airways and alveoli (c, f, h), edema (c, d, g, I, k), and perivascular cuffing (j). A normal region of a mouse lung at the $5 \times 10^3$ PFU dose is shown (l). Image (a) was captured at 10X magnification and all other images were acquired at 40X magnification. Images are representative of at least 3 samples. Scale bars in lower right corners of each panel are 1 mm.

**Table 2**
maM35c4 mutations.

| MERS region/protein | Type of mutation in maM35c4 clone | Amino acid position | Nucleotide change | Nucleotide numbering |
|---|---|---|---|---|
| 5′ UTR | single nucleotide change | N/A | CTCACTT → CTCGCTT | 28 |
| nsp3 | Missense | A217V | GCA → GTA | 3486–3488 |
| nsp3 | Missense | T1615N | ACT → AAT | 7680–7682 |
| nsp6 | Missense | L232F | CTT → TTT | 11631–11633 |
| nsp8[a] | Missense | I108L | ATT → CTT | 12384–12386 |
| nsp14 | Missense | T521I | ACA → ATA | 19562–19564 |
| spike | Missense | N222Y | AAT → TAT | 22119–22121 |
| spike[a] | Insertion of RMR | R884-RMR-S885L | AATGCGGCT | 24109\|\|24110 |
| spike[a] | Missense | S885L (L is 888 in new sequence) | AGT → CTT | 24108–24110 |
| Orf3 | Nonsense | Q4stop | CAA → TAA | 25541–25543 |
| Orf4a | Missense | P85L | CCT → CTT | 26104–26106 |
| Orf4b/Orf5 | Large deletion between Orf4b & Orf5 | N/A | GATTTT...Δ...AAACCC | 26211–26863 |
| Membrane | Missense | S2F | TCT → TTT | 27856–27858 |

Protein and nucleotide sequence numbering is based on the EMC 2012 sequence (JX869059.2) with nonstructural protein annotations described in NC_019843
Numbering for the amino acids begins with the first amino acid of each individual protein.

[a] Mutations that can also be found in icMERSma1 (Cockrell et al., 2016).

### 3.2. *Mouse-adapted M35c4 nonstructural protein mutations*

The orf1a/1b genomic regions are conserved throughout the *Coronaviridae* family and encode 16 nonstructural proteins (nsp's) that compose the replication and transcription complex. Mouse-adapted M35c4 acquired unique mutations in several non-structural proteins including nsp3, nsp6, nsp8 and nsp14, including novel missense mutations in nsp3, nsp6, and nsp14 as compared to icMERSma1. Curiously, the mutation in nsp8 (I108L) remained fixed following an additional 20 rounds of adaptive evolution. An isoleucine to leucine mutations could be considered a minor exchange of two hydrophobic residues that may have little impact on nsp8 functions in fidelity and processivity, especially considering that a hydrophobic residue at this position is conserved across many coronaviruses [see alignment in (Subissi et al., 2014)]. The nsp8 from severe acute respiratory syndrome coronavirus (SARS-CoV) was demonstrated to form a tripartite complex with nsp7 and nsp12, and confer processivity to the RNA synthesizing activity of nsp12 (Subissi et al., 2014). The nsp8/nsp12 interaction was found to be critical for RNA-dependent RNA polymerase activity of nsp12 (Subissi et al., 2014). At this time, it is not clear whether the I108L mutation impacts virus processivity or alters pathogenesis of MERS-CoV by some other mechanism. For example, Subissi *et al.* also demonstrate that the nsp7/nsp8/nsp12 tripartite complex associates with nsp14 to augment the fidelity of viral replication by commandeering the proofreading mechanism of the exoribonuclease and the N7-methyltransferase activities (N7-MTase) (Subissi et al., 2014). In addition, we identified a missense mutation (T521I) in the N7-methyltransferase domain of nsp14. A number of studies have investigated the impact of mutations across nsp14 on coronavirus replication [reviewed in (Snijder et al., 2016)]. Although it is not clear whether mutations in

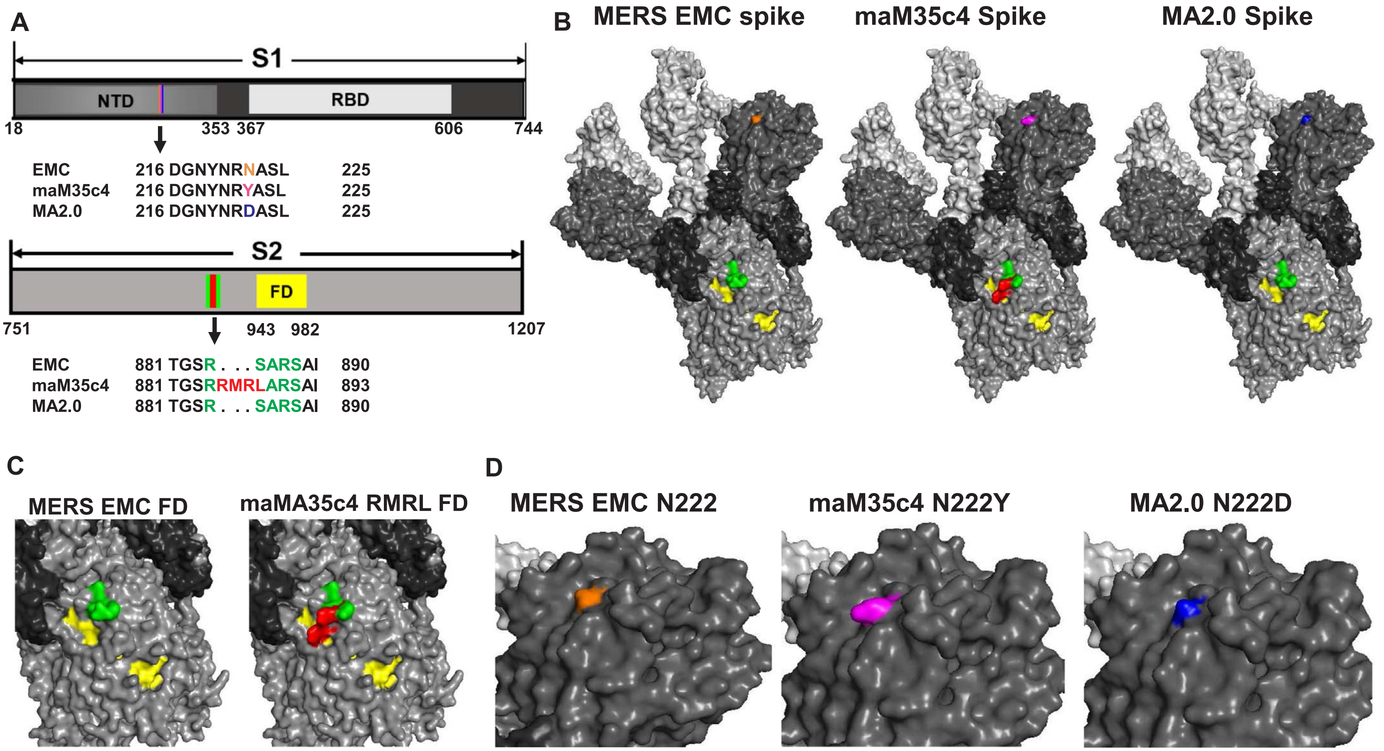

Figure 5

**Fig. 5. Structural modeling of the maM35c4 spike mutations against EMC 2012 and MA2.0.** a. Alignment of the amino acid sequences identified in the S1 and S2 domains from EMC 2012, maM35c4, and MA2.0. The colors in S1 correspond to amino acid sequence changes in the N-terminal domains (NTD) of maM35c4 (magenta, N222Y), and MA2.0 (blue, N222D) compared to EMC 2012 (orange). In the S2 domain the RMR insertion and S885L mutations in maM35c4 (red) are compared to the wild-type sequence in EMC 2012 and MA2.0 (green). The S2′ fusion domain region is highlighted in yellow. Varying shades of light gray to black in the S1 and S2 diagrams correspond with the same coloring scheme depicted for the spike trimers in (b). b. Structural modeling of MERS-CoV monomers was conducted using the PHYRE2 online modeling software; trimers were constructed using the PyMOL Molecular Graphics System. All the respective mutations identified within the spikes of maM35c4 and MA2.0 were incorporated into the modeled structure. The additional mutations in MA2.0 are not visible on the surface of the structure as shown. c and d. Expanded views of the structural regions observed near the S2′ and fusion domains of EMC 2012 and maM35c4 (c) and the region of the NTD encompassing amino acid N222 from EMC 2012, maM35c4, and MA2.0 (d).

nsp8 and nsp14 influence MERS-CoV pathogenesis, future studies are warranted to investigate the role of these changes in disease.

Although the missense mutation in nsp6 (L232F) of maM35c4 was novel in this study, a different mutation in nsp6 was identified in the icMERSma1 virus (T184I) (Cockrell et al., 2016), implicating nsp6 as an important MERS-CoV genetic locus for acquiring mutations during adaptive evolution in mice. The nsp6 protein from SARS-CoV has been demonstrated to be involved in the formation of double-membrane vesicles (DMVs) that anchor membrane-bound replication complexes (Angelini et al., 2013). Lundin et al. recently demonstrated that an inhibitor, K22, selectively targets DMVs formation in HCoV-229E infected cells and selects for resistance mutations in nsp6 (Lundin et al., 2014). As K22 also inhibits MERS-CoV replication *in vitro* (Lundin et al., 2014), nsp6 mutations might enhance virus replication and pathogenesis *in vivo* and requires additional study. Evaluating the effect of K22 on the mouse-adapted nsp6 mutations, compared to wild-type nsp6, will be the subject of future *in vitro* and *in vivo* studies.

Mouse-adapted M35c4 revealed two novel missense mutations in nsp3 (A217V and T1615N). The nsp3 protein is a multi-domain protein with multiple functions as indicated for SARS-CoV (Baez-Santos et al., 2015). Using the SARS-CoV model as a guide, the A217V mutation likely resides in the catalytically active ADP-ribose-1″-phosphatase domain (ADRP domain, a.k.a. macro domain or X domain) (Baez-Santos et al., 2015), and the T1615N mutation would reside in the Y domain toward the carboxy terminus of nsp3 (Baez-Santos et al., 2015). These domains remain largely uncharacterized, with the exception of the crystal structure of the ADRP domain being solved for SARS-CoV, and *in vitro* assays confirming the nsp3 phosphatase activity (Egloff et al., 2006; Saikatendu et al., 2005). Moreover, mutations in the catalytic domain of ADRP alter pathogenesis, but not replication, suggesting that these mutations may play important roles in virus-host interactions and disease (Fehr et al., 2015).

Importantly, our data is further supported by the discovery of mutations in nsp3, nsp6, and nsp14 that were independently identified in a different mouse-adapted MERS-CoV (Li et al., 2017a). Independent verification is strongly suggestive that mutations in these nsps play a critical role in MERS-CoV pathogenesis and the development of severe respiratory disease. Clearly, panels of recombinant viruses will be needed to unravel the role of each of the nsp mutations in virus replication and pathogenesis *in vivo*.

### 3.3. *Mouse-adapted M35c4 conserved spike mutations*

As the primary determinant of MERS-CoV tropism, changes in the spike protein are of particular interest when evaluating mouse-adapted coronaviruses. We noted that the spike protein of maM35c4 included a missense mutation at a putative glycosylation site (N222Y). Similarly, Li et al. also observed a mutation at the same position (N222D). Structural predictions showed minor differences in the structural modification between the two mutants (Fig. 5b,d). Although a change from a nonpolar, uncharged tyrosine residue to a negatively charged, aspartic acid residue, may have differing functional consequences, the common theme between these independently acquired mutations is the loss of a putative glycosylation site at this position. The N222 position resides in the N-terminal domain of S1 and is structurally distinct from the receptor binding domain (Fig. 5b), which is the major determinant of viral tropism through interaction with DPP4 (Hulswit et al., 2016). Recent studies have shown that the coronavirus S1 domain folds into 4 distinct subdomains referred to as S1$^A$ – S1$^D$ (Kirchdoerfer et al., 2016; Walls et al., 2016). The N222 mutation is positioned within the S1$^A$ subdomain, which was recently demonstrated to support a predominant interaction with host α2,3-linked sialic acid relative to interaction with α2,6-linked sialic acid (Li et al., 2017b). The distribution of host α2,3-linked sialic acid residues in humans and camels correlates with MERS-CoV infections in the lower and upper respiratory tract of each of the respective species (Li et al., 2017b; Widagdo et al., 2016). It was proposed that the α2,3-linked sialic acid residues may facilitate an initial low affinity interaction with cells, prior to a high affinity interaction between the RBD in S1$^B$ and host DPP4 receptor (Li et al., 2017b). Elimination of the putative N222 glycosylation site through adaptive evolution in the mouse may influence the initial interaction with sialic acid residues, possibly enhancing infection or expanding host cell tropism.

The S1 domain is proteolytically separated from the S2 domain by a furin cleavage at the S1/S2 interface (Millet and Whittaker, 2014). A second furin cleavage site is thought to be cleaved upon viral entry and is referred to as S2′ (Millet and Whittaker, 2014). Mouse-adapted M35c4 has an RMR insertion and S885L mutations in the S2 domain of the MERS spike. These mutations were originally acquired from passaging on murine NIH 3T3 cells in tissue culture (Cockrell et al., 2016) and remained fixed through all 35 rounds of adaptive evolution in the mouse. Placing our mutations in the context of the MERS-CoV spike trimer demonstrated that these mutations disrupt the canonical S2′ cleavage site in EMC 2012. Nonetheless, using cleavage site prediction software it appears that these mutations created a novel furin recognition site. We previously demonstrated that a MERS-CoV strain harboring only these mutations (MERS-0), can replicate with faster kinetics in tissue culture and to higher titers than EMC 2012 in mouse lungs (Cockrell et al., 2016). We suspect that the novel furin cleavage site is more amenable to processing by mouse furin and thereby can enhance the kinetics of viral replication, but this remains to be tested. Importantly, the mutations in S2 alone were not sufficient to elicit respiratory disease, even at high ($5 \times 10^6$ PFU) viral doses (Cockrell et al., 2016). Therefore, a combination of mouse-adapted mutations may be necessary to elicit severe respiratory disease.

### 3.4. Mouse-adapted M35c4 mutations in accessory ORFs and the M protein

A number of studies have implicated the MERS-CoV accessory ORFs (ORF4a, ORF4b, ORF5) and M protein as potential antagonists of the innate immune response (Matthews et al., 2014; Menachery et al., 2017; Rabouw et al., 2016; Thornbrough et al., 2016; Yang et al., 2015, 2013). We identified a large deletions in ORF4b that extended through the beginning of ORF5, essentially eliminating expression of these proteins. Li et al. also identified a large deletion in ORF5, as well as a number of other ORF deletions, in their mouse-adapted viruses (Li et al., 2017a). Expression of ORF3 from maM35c4 was also eliminated since a nonsense mutation (Q4stop) was identified at the 5′ end of the protein. Additionally, we identified a missense mutation (P85L) in ORF4a, which is outside putative RNA binding domains. Considering all the accessory ORFs, only ORF4a appears to be expressed from maM35c4. ORF3, much of ORF4b and ORF5 appear to be dispensable for MERS-CoV pathogenesis in mouse lungs. Nonetheless, Menachery et al. demonstrate that using an infectious clone of the icMERSma1 virus with complete deletion of ORFs 3–5 resulted in attenuation in mice (Menachery et al., 2017). If we combine this observation with data from our current maM35c4 isolate we can speculate that ORF4a may act as a strong interferon antagonist in mice to facilitate development of severe respiratory disease. Interestingly, MERS-CoV isolates have also been obtained from human patients with deletions in ORF3 and ORF4a; albeit, only 16 amino acids were deleted from ORF4a (Lamers et al., 2016).

*In vitro* studies have also demonstrated that the MERS-CoV M protein may function as an interferon antagonist (Lui et al., 2016; Yang et al., 2013). The N terminal regions from SARS-CoV and MERS-CoV M proteins were shown to be sufficient to inhibit interferon expression (Lui et al., 2016; Siu et al., 2014). In the case of MERS-CoV the N-terminus of the M protein was found to interact with TRAF3 and disrupt the TRAF3-TBK1 association that leads to IRF3 activation (Lui et al., 2016). We identified a missense mutation (S2F) at the N-terminus of the M protein. Li et al. (2017a) also identified a missense mutation at the N-terminus of the M protein in their mouse-adapted MERS-CoV. Missense mutations at the N-terminus of SARS-CoV M protein have also been associated with increased pathogenesis in mice (Roberts et al., 2007), and enhanced virus production following adaptation in tissue culture (Pacciarini et al., 2008). Taken together, these studies imply that MERS-CoV and SARS-CoV may share conserved functions that reside in the M protein N-terminus that may contribute to pathogenesis in mice.

## 4. Conclusion

We have developed a robust mouse model for MERS-CoV pathogenesis that recapitulates lethal end stage lung phenotypes after low dose challenge. In addition to achieving a low challenge dose, continued adaptive evolution identified conserved, and novel mutations, throughout the MERS-CoV genome that may have functional implications regarding the phenotypes observed during infection. Future studies will include the generation of a MERS-CoV infectious clone containing all the mutations to confirm the observed disease phenotypes at the infectious doses described in this study; and, the subsequent generation of novel viruses with different combinations of mutations to evaluate their role in replication and severe respiratory disease. As disease pathology replicates many of the end stage lung disease phenotypes seen in humans, this model will be valuable for evaluating pathogenic mechanisms of MERS-CoV, host immune responses to MERS-CoV, and the use of therapeutics and vaccines to reverse disease signatures.

## 5. Materials and methods

Unless otherwise indicated details for each of the following headings can be found in (Cockrell et al., 2016)

### 5.1. Cells and viruses

Maintenance and preparation of cells and virus stocks can be found in (Cockrell et al., 2016).

### 5.2. Mouse infections

All infections were done as previously described in 288–330$^{+/-}$ or 288–330$^{+/+}$ mice (Cockrell et al., 2016). Briefly, since the 288–330+/+ mice are novel mouse lines developed and bred in the Baric lab, experiments utilized available male and female mice that ranged 18–22 weeks of age. Mice were randomly included into cohorts at the indicated time points. Mouse studies were executed under ABSL3 conditions. Prior to viral infection mice were anesthetized by administering 50ul of a ketamine/xylazine mixture intraperitoneally, and then infected intranasally with a 50ul volume of virus at the indicated dose. Following sedation and infection mice were monitored daily for weight loss and survival, as well as signs that animals were moribund (including labored breathing, lack of movement, and lack of grooming). Mice that reached 20% weight loss were placed under exception, and monitored at least three times daily. Mice that approached 30% weight loss were immediately euthanized. Mice deemed moribund were euthanized at the discretion of the researcher. Mice were euthanized with an isoflurane overdose followed by a secondary thoracotomy, at the time points indicated in the results, for collecting lung tissues. All methods are approved methods of the Institutional Animal Care and Use Committee (IACUC) at The University of North Carolina at Chapel

Hill.

### 5.3. Ethics statement

Mouse studies were carried out in accordance with the recommendations for the care and use of animals by the Office of Laboratory Animal Welfare at NIH. IACUC at UNC-CH approved the animal studies performed here (protocol, IACUC 16–251), using a weight loss cut-off point of ~30% for humane euthanasia.

### 5.4. Continued adaptation of icMERSma1 in 288–330$^{+/-}$ heterozygous mice

GOF research considerations involving MERS-CoV *in vivo* passage in mice were reviewed and approved by the funding agency, the NIH, during the award period. All passaging experiments were executed during the award period. Passaging through mouse lungs of 288–330$^{+/-}$ mice was continued with MERS-15 C2, the infectious clone of which is referred to as icMERSma1 as described previously (Cockrell et al., 2016). Passaging was continued an additional 10 or 20 times to establish the MERS-25 and MERS-35 isolates, respectively. Clonal isolates of the MERS-35 virus were obtained by plaque purification and amplification in Vero CCL81 cells. After confirming that the maM35c4 clonal isolate elicited signs indicative of respiratory disease, RNA was extracted from the lung of an infected mouse and sequenced by RT-PCR. Briefly, RNA was extracted from lungs according to the manufacturer's instructions for TRIzol Reagent (Invitrogen). Reverse transcription reactions were performed using SuperScript III first-strand synthesis system for RT-PCR (Invitrogen) following by amplification with Phusion high fidelity DNA polymerase (New England BioLads), according to manufacturer's instructions. To obtain the 5′ ends of capped viral RNAs we used the FirstChoice RLM-RACE kit (ThermoFisher) according to manufacturer's instructions. All sequencing was out-sourced off-site to Eurofins Genomics. Characterization of the mouse-adapted M35c4 strain was executed at 10–1000 fold lower titers, where indicated, than previously used for the icMERSma1 strain.

### 5.5. Histology

Lung tissue sections were processed and stained at the Lineberger Comprehensive Cancer Center Animal Histopathology Core facility at UNC-CH, as previously described (Cockrell et al., 2016).

### 5.6. Statistical analysis

All quantitative data are presented as means ± S.E.M. Significance between specific data sets is described in the respective figure legends and was determined by multiple Student's *t*-test function in GraphPad Prism 7.0. Since this function was used to make single comparisons between indicated groups a correction for multiple comparisons was not used and the alpha value was set at 0.05 (definition of statistically significant).

### 5.7. Homology structural modeling

The spike sequences of the MERS-CoVs EMC 2012 (GenBank Accession number: JX869059.2), maM35c4, and MA2.0 (Li et al., 2017a) were analyzed using the Protein Homology/analogy Recognition Engine V2.0 (PHYRE2) server (Kelley et al., 2015). The submitted sequences included the noted mutations in the N-terminal domains and S2′ furin cleavage site of maM35c4 and MA2.0. The monomeric spike subunits were modeled into MERS-CoV trimers based on the prefusion structure (RCSB PDB ID: 5 × 59) (Yuan et al., 2017) using the PyMOL Molecular Graphics System, Version 1.7.3.4 Schrodinger LLC. The models predicted with the Protein Homology/analogy Recognition Engine V2.0 (PHYRE2) server were further validated using different software including the MPI Bioinformatics toolkit and the SWISS-MODEL server from the SIB Bioinformatics Resource Portal. Due to redundancy in the models only the model based upon the PHYRE 2 software is included in the manuscript.

### 5.8. Biosafety and biosecurity

A detailed description is available in Cockrell et al. (2016). Regarding continuation of gain-of-function experiments. *In vivo* adaptation is in accordance with our US NIH award HHSN272201000019I-HHSN27200003 (R.S.B.). Work for this study is agreement with receipt of our exemption from the US Government's statement on funding pause for certain types of GOF research.

### 5.9. Data availability

The data that support the findings of this study are available from the corresponding authors on request

## Acknowledgements

These studies were supported by grants from the National Institute of Allergy and Infectious Disease of the US NIH by awards HHSN272201000019I-HHSN27200003 (R.S.B.), AI110700, and AI089728 (R.S.B.). The content is solely the responsibility of the authors and does necessarily represent the official views of the NIH.

## Author contributions

M.G.D. wrote the manuscript, executed experiments, and analyzed data. J.F.K. performed structural analysis for the spike proteins. T.S. prepared RNA and analyzed sequencing data for viruses. R.S.B. conceived/designed experiments and wrote manuscript. A.S.C. conceived /designed the experiments, performed experiments, analyzed data, and wrote the manuscript.

## Competing interests

The authors declare no competing financial interests.

## Appendix A. Supporting information

Supplementary data associated with this article can be found in the online version at http://dx.doi.org/10.1016/j.virol.2017.12.006.

## References

Alsaad, K.O., Hajeer, A.H., Al Balwi, M., Al Moaiqel, M., Al Oudah, N., Al Ajlan, A., AlJohani, S., Alsolamy, S., Gmati, G.E., Balkhy, H., Al-Jahdali, H.H., Baharoon, S.A., Arabi, Y.M., 2017. Histopathology of Middle East respiratory syndrome coronovirus (MERS-CoV) infection - clinicopathological and ultrastructural study. Histopathology.

Angelini, M.M., Akhlaghpour, M., Neuman, B.W., Buchmeier, M.J., 2013. Severe acute respiratory syndrome coronavirus nonstructural proteins 3, 4, and 6 induce double-membrane vesicles. mBio 4.

Arabi, Y.M., Balkhy, H.H., Hayden, F.G., Bouchama, A., Luke, T., Baillie, J.K., Al-Omari, A., Hajeer, A.H., Senga, M., Denison, M.R., Nguyen-Van-Tam, J.S., Shindo, N., Bermingham, A., Chappell, J.D., Van Kerkhove, M.D., Fowler, R.A., 2017. Middle east respiratory syndrome. N. Engl. J. Med. 376, 584–594.

Baez-Santos, Y.M., St John, S.E., Mesecar, A.D., 2015. The SARS-coronavirus papain-like protease: structure, function and inhibition by designed antiviral compounds. Antivir. Res. 115, 21–38.

Bin, S.Y., Heo, J.Y., Song, M.S., Lee, J., Kim, E.H., Park, S.J., Kwon, H.I., Kim, S.M., Kim, Y.I., Si, Y.J., Lee, I.W., Baek, Y.H., Choi, W.S., Min, J., Jeong, H.W., Choi, Y.K., 2016. Environmental contamination and viral shedding in MERS patients during MERS-CoV outbreak in South Korea. Clin. Infect. Dis. 62, 755–760.

Chan, J.F., Yao, Y., Yeung, M.L., Deng, W., Bao, L., Jia, L., Li, F., Xiao, C., Gao, H., Yu, P., Cai, J.P., Chu, H., Zhou, J., Chen, H., Qin, C., Yuen, K.Y., 2015. Treatment With Lopinavir/Ritonavir or interferon-beta1b improves outcome of MERS-CoV infection in a nonhuman primate model of common marmoset. J. Infect. Dis. 212, 1904–1913.

Cockrell, A.S., Yount, B.L., Scobey, T., Jensen, K., Douglas, M., Beall, A., Tang, X.C., Marasco, W.A., Heise, M.T., Baric, R.S., 2016. A mouse model for MERS coronavirus-induced acute respiratory distress syndrome. Nat. Microbiol. 2, 16226.

Coleman, C.M., Sisk, J.M., Halasz, G., Zhong, J., Beck, S.E., Matthews, K.L., Venkataraman, T., Rajagopalan, S., Kyratsous, C.A., Frieman, M.B., 2017. CD8+ T cells and macrophages regulate pathogenesis in a mouse model of middle east respiratory syndrome. J. Virol. 91.

Egloff, M.P., Malet, H., Putics, A., Heinonen, M., Dutartre, H., Frangeul, A., Gruez, A., Campanacci, V., Cambillau, C., Ziebuhr, J., Ahola, T., Canard, B., 2006. Structural and functional basis for ADP-ribose and poly(ADP-ribose) binding by viral macro domains. J. Virol. 80, 8493–8502.

Falzarano, D., de Wit, E., Feldmann, F., Rasmussen, A.L., Okumura, A., Peng, X., Thomas, M.J., van Doremalen, N., Haddock, E., Nagy, L., LaCasse, R., Liu, T., Zhu, J., McLellan, J.S., Scott, D.P., Katze, M.G., Feldmann, H., Munster, V.J., 2014. Infection with MERS-CoV causes lethal pneumonia in the common marmoset. PLoS Pathog. 10, e1004250.

Fehr, A.R., Athmer, J., Channappanavar, R., Phillips, J.M., Meyerholz, D.K., Perlman, S., 2015. The nsp3 macrodomain promotes virulence in mice with coronavirus-induced encephalitis. J. Virol. 89, 1523–1536.

Hulswit, R.J., de Haan, C.A., Bosch, B.J., 2016. Coronavirus spike protein and tropism changes. Adv. Virus Res. 96, 29–57.

Johnson, R.F., Via, L.E., Kumar, M.R., Cornish, J.P., Yellayi, S., Huzella, L., Postnikova, E., Oberlander, N., Bartos, C., Ork, B.L., Mazur, S., Allan, C., Holbrook, M.R., Solomon, J., Johnson, J.C., Pickel, J., Hensley, L.E., Jahrling, P.B., 2015. Intratracheal exposure of common marmosets to MERS-CoV Jordan-n3/2012 or MERS-CoV EMC/2012 isolates does not result in lethal disease. Virology 485, 422–430.

Johnson, R.F., Bagci, U., Keith, L., Tang, X., Mollura, D.J., Zeitlin, L., Qin, J., Huzella, L., Bartos, C.J., Bohorova, N., Bohorov, O., Goodman, C., Kim do, H., Paulty, M.H., Velasco, J., Whaley, K.J., Johnson, J.C., Pettitt, J., Ork, B.L., Solomon, J., Oberlander, N., Zhu, Q., Sun, J., Holbrook, M.R., Olinger, G.G., Baric, R.S., Hensley, L.E., Jahrling, P.B., Marasco, W.A., 2016. 3B11-N, a monoclonal antibody against MERS-CoV, reduces lung pathology in rhesus monkeys following intratracheal inoculation of MERS-CoV Jordan-n3/2012. Virology 490, 49–58.

Kelley, L.A., Mezulis, S., Yates, C.M., Wass, M.N., Sternberg, M.J., 2015. The Phyre2 web portal for protein modeling, prediction and analysis. Nat. Protoc. 10, 845–858.

Kirchdoerfer, R.N., Cottrell, C.A., Wang, N., Pallesen, J., Yassine, H.M., Turner, H.L., Corbett, K.S., Graham, B.S., McLellan, J.S., Ward, A.B., 2016. Pre-fusion structure of a human coronavirus spike protein. Nature 531, 118–121.

Lamers, M.M., Raj, V.S., Shafei, M., Ali, S.S., Abdallh, S.M., Gazo, M., Nofal, S., Lu, X., Erdman, D.D., Koopmans, M.P., Abdallat, M., Haddadin, A., Haagmans, B.L., 2016. Deletion variants of middle east respiratory syndrome coronavirus from humans, Jordan, 2015. Emerg. Infect. Dis. 22, 716–719.

Lee, S.I., 2015. Costly lessons from the 2015 middle east respiratory syndrome coronavirus outbreak in Korea. J. Prev. Med. Public Health 48, 274–276.

Li, K., Wohlford-Lenane, C.L., Channappanavar, R., Park, J.E., Earnest, J.T., Bair, T.B., Bates, A.M., Brogden, K.A., Flaherty, H.A., Gallagher, T., Meyerholz, D.K., Perlman, S., McCray Jr., P.B., 2017a. Mouse-adapted MERS coronavirus causes lethal lung disease in human DPP4 knockin mice. Proc. Natl. Acad. Sci. USA 114, E3119–E3128.

Li, W., Hulswit, R.J.G., Widjaja, I., Raj, V.S., McBride, R., Peng, W., Widagdo, W., Tortorici, M.A., van Dieren, B., Lang, Y., van Lent, J.W.M., Paulson, J.C., de Haan, C.A.M., de Groot, R.J., van Kuppeveld, F.J.M., Haagmans, B.L., Bosch, B.J., 2017b. Identification of sialic acid-binding function for the Middle East respiratory syndrome coronavirus spike glycoprotein. Proc. Natl. Acad. Sci. USA.

Lui, P.Y., Wong, L.Y., Fung, C.L., Siu, K.L., Yeung, M.L., Yuen, K.S., Chan, C.P., Woo, P.C., Yuen, K.Y., Jin, D.Y., 2016. Middle East respiratory syndrome coronavirus M protein suppresses type I interferon expression through the inhibition of TBK1-dependent phosphorylation of IRF3. Emerg. Microbes Infect. 5, e39.

Lundin, A., Dijkman, R., Bergstrom, T., Kann, N., Adamiak, B., Hannoun, C., Kindler, E., Jonsdottir, H.R., Muth, D., Kint, J., Forlenza, M., Muller, M.A., Drosten, C., Thiel, V., Trybala, E., 2014. Targeting membrane-bound viral RNA synthesis reveals potent inhibition of diverse coronaviruses including the middle East respiratory syndrome virus. PLoS Pathog. 10, e1004166.

Matthews, K.L., Coleman, C.M., van der Meer, Y., Snijder, E.J., Frieman, M.B., 2014. The ORF4b-encoded accessory proteins of Middle East respiratory syndrome coronavirus and two related bat coronaviruses localize to the nucleus and inhibit innate immune signalling. J. Gen. Virol. 95, 874–882.

Menachery, V.D., Mitchell, H.D., Cockrell, A.S., Gralinski, L.E., Yount Jr., B.L., Graham, R.L., McAnarney, E.T., Douglas, M.G., Scobey, T., Beall, A., Dinnon 3rd, K., Kocher, J.F., Hale, A.E., Stratton, K.G., Waters, K.M., Baric, R.S., 2017. MERS-CoV accessory ORFs play key role for infection and pathogenesis. mBio 8.

Meyerholz, D.K., Lambertz, A.M., McCray Jr., P.B., 2016. Dipeptidyl peptidase 4 distribution in the human respiratory tract: implications for the middle east respiratory syndrome. Am. J. Pathol. 186, 78–86.

Millet, J.K., Whittaker, G.R., 2014. Host cell entry of Middle East respiratory syndrome coronavirus after two-step, furin-mediated activation of the spike protein. Proc. Natl. Acad. Sci. USA 111, 15214–15219.

Munster, V.J., de Wit, E., Feldmann, H., 2013. Pneumonia from human coronavirus in a macaque model. N. Engl. J. Med. 368, 1560–1562.

Ng, D.L., Al Hosani, F., Keating, M.K., Gerber, S.I., Jones, T.L., Metcalfe, M.G., Tong, S., Tao, Y., Alami, N.N., Haynes, L.M., Mutei, M.A., Abdel-Wareth, L., Uyeki, T.M., Swerdlow, D.L., Barakat, M., Zaki, S.R., 2016. Clinicopathologic, immunohistochemical, and ultrastructural findings of a fatal case of middle east respiratory syndrome coronavirus infection in the United Arab Emirates, April 2014. Am. J. Pathol. 186, 652–658.

Oh, M.D., Park, W.B., Choe, P.G., Choi, S.J., Kim, J.I., Chae, J., Park, S.S., Kim, E.C., Oh, H.S., Kim, E.J., Nam, E.Y., Na, S.H., Kim, D.K., Lee, S.M., Song, K.H., Bang, J.H., Kim, E.S., Kim, H.B., Park, S.W., Kim, N.J., 2016. Viral load kinetics of MERS coronavirus infection. N. Engl. J. Med. 375, 1303–1305.

Ohnuma, K., Dang, N.H., Morimoto, C., 2008. Revisiting an old acquaintance: CD26 and its molecular mechanisms in T cell function. Trends Immunol. 29, 295–301.

Pacciarini, F., Ghezzi, S., Canducci, F., Sims, A., Sampaolo, M., Ferioli, E., Clementi, M., Poli, G., Conaldi, P.G., Baric, R., Vicenzi, E., 2008. Persistent replication of severe acute respiratory syndrome coronavirus in human tubular kidney cells selects for adaptive mutations in the membrane protein. J. Virol. 82, 5137–5144.

Rabouw, H.H., Langereis, M.A., Knaap, R.C., Dalebout, T.J., Canton, J., Sola, I., Enjuanes, L., Bredenbeek, P.J., Kikkert, M., de Groot, R.J., van Kuppeveld, F.J., 2016. Middle east respiratory coronavirus accessory protein 4a inhibits PKR-mediated antiviral stress responses. PLoS Pathog. 12, e1005982.

Roberts, A., Deming, D., Paddock, C.D., Cheng, A., Yount, B., Vogel, L., Herman, B.D., Sheahan, T., Heise, M., Genrich, G.L., Zaki, S.R., Baric, R., Subbarao, K., 2007. A mouse-adapted SARS-coronavirus causes disease and mortality in BALB/c mice. PLoS Pathog. 3, e5.

Rohrborn, D., Wronkowitz, N., Eckel, J., 2015. DPP4 in diabetes. Front. Immunol. 6, 386.

Saikatendu, K.S., Joseph, J.S., Subramanian, V., Clayton, T., Griffith, M., Moy, K., Velasquez, J., Neuman, B.W., Buchmeier, M.J., Stevens, R.C., Kuhn, P., 2005. Structural basis of severe acute respiratory syndrome coronavirus ADP-ribose-1"-phosphate dephosphorylation by a conserved domain of nsP3. Structure 13, 1665–1675.

Siu, K.L., Chan, C.P., Kok, K.H., Chiu-Yat Woo, P., Jin, D.Y., 2014. Suppression of innate antiviral response by severe acute respiratory syndrome coronavirus M protein is mediated through the first transmembrane domain. Cell Mol. Immunol. 11, 141–149.

Snijder, E.J., Decroly, E., Ziebuhr, J., 2016. The nonstructural proteins directing coronavirus RNA synthesis and processing. Adv. Virus Res. 96, 59–126.

Subissi, L., Posthuma, C.C., Collet, A., Zevenhoven-Dobbe, J.C., Gorbalenya, A.E., Decroly, E., Snijder, E.J., Canard, B., Imbert, I., 2014. One severe acute respiratory syndrome coronavirus protein complex integrates processive RNA polymerase and exonuclease activities. Proc. Natl. Acad. Sci. USA 111, E3900–E3909.

Thornbrough, J.M., Jha, B.K., Yount, B., Goldstein, S.A., Li, Y., Elliott, R., Sims, A.C., Baric, R.S., Silverman, R.H., Weiss, S.R., 2016. Middle east respiratory syndrome coronavirus NS4b protein inhibits host RNase L activation. mBio 7, e00258.

Walls, A.C., Tortorici, M.A., Bosch, B.J., Frenz, B., Rottier, P.J.M., DiMaio, F., Rey, F.A., Veesler, D., 2016. Cryo-electron microscopy structure of a coronavirus spike glycoprotein trimer. Nature 531, 114–117.

WHO, 2017. WHO | Middle East respiratory syndrome coronavirus (MERS-CoV). 〈http://www.who.int/emergencies/mers-cov/en/〉.

Widagdo, W., Raj, V.S., Schipper, D., Kolijn, K., van Leenders, G.J., Bosch, B.J., Bensaid, A., Segales, J., Baumgartner, W., Osterhaus, A.D., Koopmans, M.P., van den Brand, J.M., Haagmans, B.L., 2016. Differential expression of the middle east respiratory syndrome coronavirus receptor in the upper respiratory tracts of humans and dromedary camels. J. Virol. 90, 4838–4842.

Yang, Y., Zhang, L., Geng, H., Deng, Y., Huang, B., Guo, Y., Zhao, Z., Tan, W., 2013. The structural and accessory proteins M, ORF 4a, ORF 4b, and ORF 5 of Middle East respiratory syndrome coronavirus (MERS-CoV) are potent interferon antagonists. Protein Cell 4, 951–961.

Yang, Y., Ye, F., Zhu, N., Wang, W., Deng, Y., Zhao, Z., Tan, W., 2015. Middle East respiratory syndrome coronavirus ORF4b protein inhibits type I interferon production through both cytoplasmic and nuclear targets. Sci. Rep. 5, 17554.

Yuan, Y., Cao, D., Zhang, Y., Ma, J., Qi, J., Wang, Q., Lu, G., Wu, Y., Yan, J., Shi, Y., Zhang, X., Gao, G.F., 2017. Cryo-EM structures of MERS-CoV and SARS-CoV spike glycoproteins reveal the dynamic receptor binding domains. Nat. Commun. 8, 15092.